

Three-dimensional Tumor Mapping in Different Orientations of Automated Breast Ultrasound

5 Chung-Ming Lo¹, Siwa Chan^{2,3}, Ya-Wen Yang⁴, Yeun-Chung Chang⁵, Yi-Sheng
Jou¹, Chiun-Sheng Huang^{4*}, and Ruey-Feng Chang^{1,2*}

10 ¹Department of Computer Science and Information Engineering
National Taiwan University, Taipei, Taiwan

²Graduate Institute of Biomedical Electronics and Bioinformatics
National Taiwan University, Taipei, Taiwan

³ Department of Radiology, Taichung Veterans General Hospital, Taichung, Taiwan

15 ⁴Department of Surgery, National Taiwan University Hospital and National Taiwan
University College of Medicine, Taipei, Taiwan

⁵Department of Medical Imaging, National Taiwan University Hospital and National
Taiwan University College of Medicine, Taipei, Taiwan

20

* Corresponding Authors:

Professor Chiun-Sheng Huang

Department of Surgery

25 National Taiwan University Hospital and National Taiwan University College of
Medicine

Taipei, Taiwan 10617, R.O.C.

Telephone: 886-2-23123456-65080

Fax: 886-2-23117100

30 E-mail: huangcs@ntu.edu.tw

Professor Ruey-Feng Chang

Department of Computer Science and Information Engineering

National Taiwan University

35 Taipei, Taiwan 10617, R.O.C.

Telephone: 886-2-33661503

Fax: 886-2-23628167

E-mail: rfchang@csie.ntu.edu.tw

40

Abstract

Purpose: An automatic tumor mapping algorithm was proposed to find the same regions in different passes of automated breast ultrasound (ABUS).

Methods: A total of 53 abnormal passes with 41 biopsy-proven tumors (25 benign
45 and 16 malignant tumors) and 13 normal passes were collected as the ABUS image database. After computer-aided tumor detection, a mapping pair is composed of a detected region in a pass and another region in another pass. Location criteria including clock, relative distance, and distance to nipple were used to extract mapping pairs with close regions. Quantitative intensity, morphology, texture, and location
50 features were then combined in a classifier to distinguish between the same and different regions in each pair.

Results : After location criteria, 92% of the original mapping pairs with different regions were reduced. The performance of the following classification achieved a mapping rate of 80.39% (41/51) with an error rate of 5.97% (4/67). The trade-offs
55 between mapping rate and error rate were evaluated using the area under receiver operating characteristic (ROC) curve and resulted in an $A_z=0.9094$.

Conclusions : The proposed tumor mapping algorithm can automatically provide location correspondence information between passes for 80% tumors which would be helpful for the efficiency of the ABUS examinations.

60 *Keywords:* Breast cancer, automated breast ultrasound, computer-aided detection,
tumor mapping

Introduction

Breast cancer has become the second leading cause of mortality for women in 2013 ¹. On clinical examination, ultrasound (US) is a popular imaging tool in the
65 detection and diagnosis of breast tumors^{2,3}. US can also be adjunct to mammography in detecting tumors in dense breasts⁴⁻⁸. However, conventional US examination is performed by hand-held and is poorly reproducible. Automated breast ultrasound (ABUS) system is developed to automatically scan the whole breast and reduce operator dependence⁴. The reproducibility of the ABUS system would be useful for
70 follow-up studies and used in screening⁴. In the scanning of the ABUS system, three passes of different orientations including anterior to posterior (AP), lateral (LAT), and medial (MED) pass are performed to completely cover a whole breast. Each pass generates a three-dimensional (3-D) image volume composed of more than 300 continuous two-dimensional (2-D) slices. The review of these image volumes is a
75 time-consuming task for radiologists. Recently, computer-aided detection (CADe) systems were developed to automatically discover suspicious abnormalities to accelerate the review procedure^{9, 10}. The CADe systems combined various quantitative intensity and shape features in a classifier to estimate the likelihoods being tumors for regions or voxels in ABUS images. The tumor detection

80 performances achieved the sensitivities from 64% to 100% with false positives (FPs) of 1 and 9.44 per pass, respectively. Whether the performance is good enough for clinical application is not yet known. Nevertheless, the tumor detection algorithms were all performed on an ABUS image volume generated in a pass of scanning. An image volume only covers a part of the whole breast therefore a tumor may exist in
85 more than one image volume and is detected more than once in the detection algorithms. The review of the same area is redundant and more time has to be spent for radiologists to determine the tumor numbers and locations.

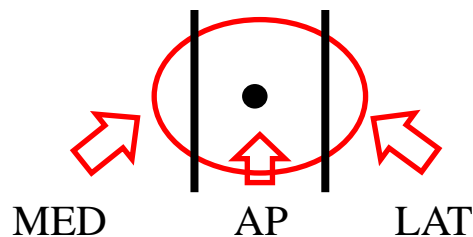
In this study, a tumor mapping algorithm was proposed to find the same regions locating in different passes. Based on the previous CADe system¹⁰, the detected
90 regions in different passes of a breast scanning were analyzed. Location criteria were first used to extract regions with similar locations relative to nipple. In the following classification, quantitative intensity, morphology, texture and location features were combined to distinguish between the same and different regions distributed in different passes. With the mapping of the same regions, more diagnostic information
95 can be obtained after tumor detection to reduce the review time of ABUS images in clinical use.

Materials and Methods

Patients and ABUS acquisition

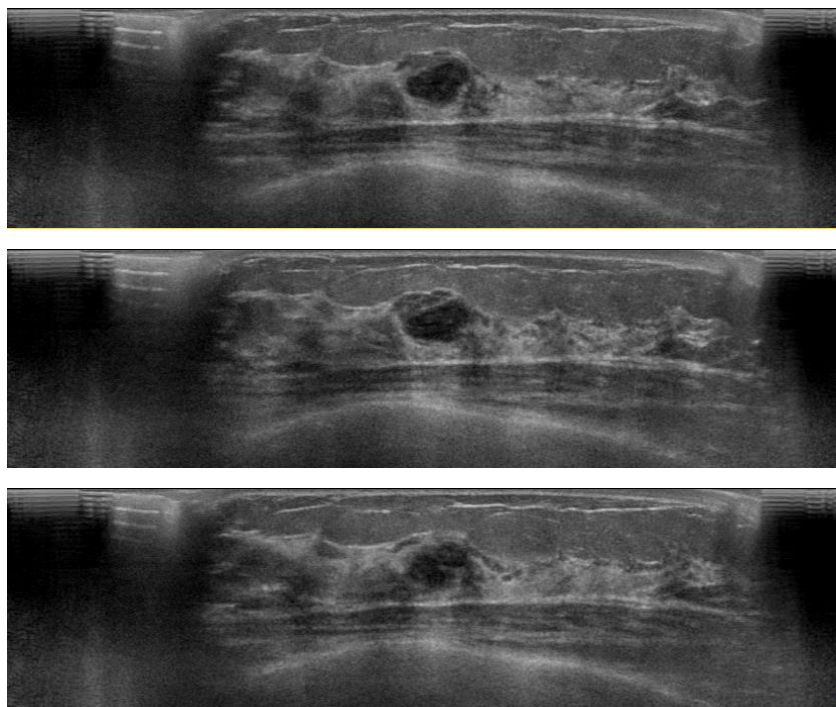
100 This retrospective study obtained patients' informed consent and approval from
our institution review board. The 66 ABUS image volumes used in the experiment
was acquired from the Breast Center of National Taiwan University Hospital between
July and December 2012. A total of 18 women (age range: 35-70 years, mean
49.35±9.06 years) underwent ABUS examination with an ACUSON S2000
105 Automated Breast Volume Scanner (Siemens Medical Solutions, Mountain View, CA,
USA) equipped with a 5 to 15 MHz linear array transducer (14L5BV). In the
examination, three passes of different orientation of breast area including AP, MED,
and LAT were performed in the scanning to completely cover the whole breast. The
patients underwent ABUS examinations were in the supine position on the examining
110 table. Each orientation scanning was performed from the lower to upper side of a
breast. In the scanning of MED or LAT orientation, the medial or lateral part of a
breast was turned to the front with compression, respectively. Fig. 1 shows the
illustration of three passes of different orientation of a breast.

115



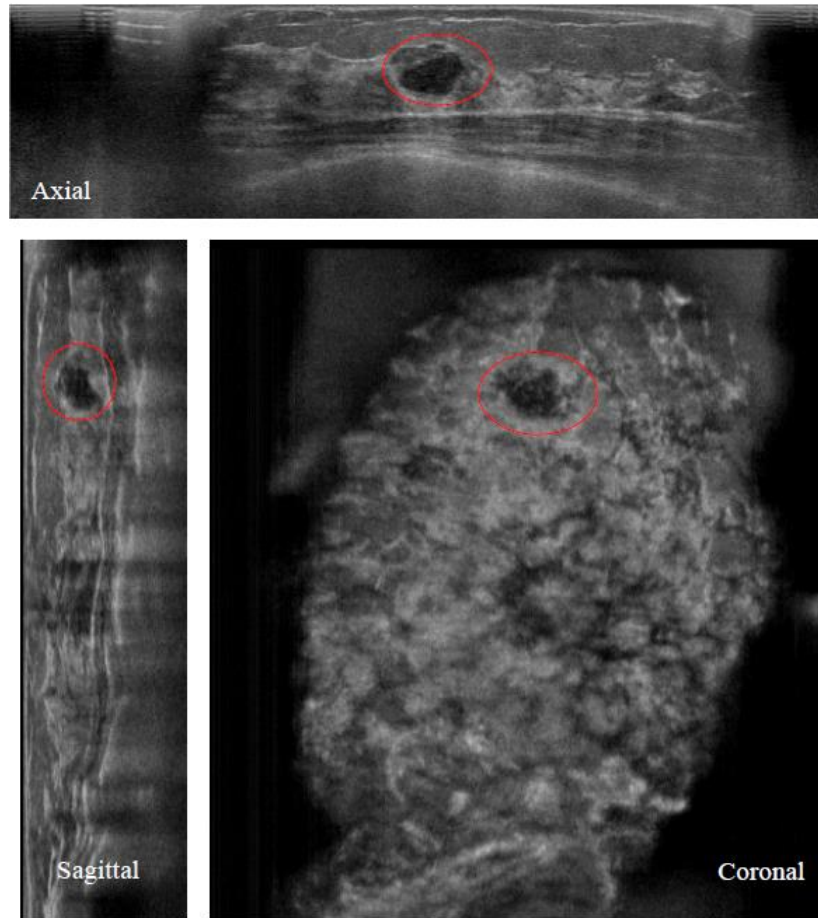
120 Fig. 1. Three passes of different orientation of a breast include AP, MED, and LAT in
the ABUS scanning for a left breast. The orientation description of MED and
LAT are exchanged for a right breast.

A pass of an orientation generated a 3-D image volume composed of 318 2-D
slices with thickness 0.5 mm. The spacing of width, height and slice was 0.0212,
0.007, and 0.052 cm/pixel, respectively. Fig. 2(a) shows a series of continuous 2-D
125 slices in an ABUS volume and (b) shows a tumor exhibited in the axial, sagittal and
coronal views.



130

(a)



(b)

Fig. 2. An ABUS image volume obtained from a 35-year-old woman with a fibroadenoma. (a) A series of 2-D slices in axial view (b) The tumor is shown in axial, sagittal, and coronal views. The circles indicate the tumor position.

135

In the collected ABUS images, 53 abnormal passes with at least one tumor and 13 normal passes were included. The 53 abnormal passes had 41 biopsy-proven lesions (size range: 0.3-7.2 cm, mean: 1.5 ± 1.3 cm) including 25 benign and 16 malignant tumors. The 25 benign tumors were 11 fibrocystic changes, 9 fibroadenoma, and 5 papilloma. The 16 malignant tumors were 13 invasive ductal carcinoma (IDC) and 3 invasive lobular carcinoma (ILC).

140

Tumor Mapping

145 The tumor mapping algorithm proposed in this study intended to find the same
regions locating in different passes to reduce the review time of ABUS images. The
regions were detected true positives (TPs) or false positives (FPs) in the CADe
system¹⁰. For the image database used in this study, the FPs/pass achieved 7.57 at the
sensitivity of 100%. That is, a total of 164 TP (tumor regions) and 347 FP (non-tumor
150 regions) were detected.

 According to the scanning procedure, the AP passes covered most breast area and
had fewer deformations than the other two passes. Therefore, regions in MED and
LAT passes were mapped to those of AP passes in the experiment. The mappings were
many-to-many mappings. Each one-to-one mapping from a MED or a LAT pass to the
155 corresponding AP pass of a breast is a pair. If there are ten regions in a MED and ten
regions in an AP pass, respectively, the mapping from the MED to AP pass is a
ten-to-ten mapping i.e. one hundred mapping pairs. Upon the CADe result, the
number of original mapping pairs was 1506. The proposed mapping algorithm aimed
at predicting whether the two regions in each mapping pair were the same according
160 to the positive and negative mapping pairs in the ground truth assessed by the
radiologist. Positive mapping pairs were mapping pairs composed of the same regions.

Negative mapping pairs were recognized as different regions.

In the tumor mapping, location criteria such as clock, relative distance, and distance to nipple of two regions in a mapping pair was first used to extract regions
165 with similar locations relative to nipple. After that, quantitative intensity, morphology, texture and location features were combined in a classifier to distinguish between the same and different regions in each pair.

The features extracted from two regions in a mapping pair were compared by the value difference. F_{diff} was the difference metric expressing the absolute value
170 difference.

$$F_{diff} = |F_A - F_B| \quad (1)$$

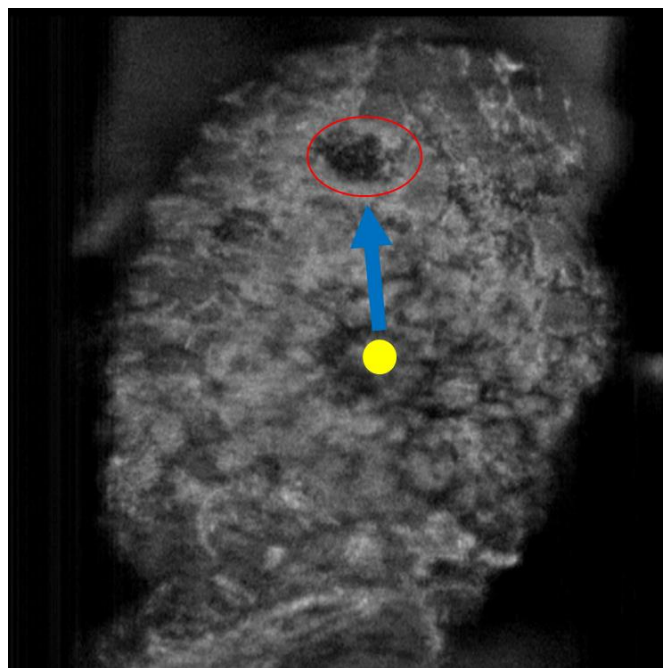
where A is the region in the AP pass and B is the region in the MED or LAT pass. F_A and F_B are the feature of region A and region B, respectively. If the feature value is too large or too small, the absolute value of difference may not reflect the difference magnitude. Another difference metric defined below is F_{diff_ratio} which takes the
175 relative difference into consideration.

$$F_{diff_ratio} = \frac{|F_A - F_B|}{F_A} \quad (2)$$

where the absolute value of feature different is divided by the feature of region A in the AP pass.

Location Criteria

180 Many mapping pairs were generated in finding the same regions between
different passes. The widely used location information on clinical examination was
calculated to describe where a region is and to reduce the number of mapping pairs.
Using the absolute coordinate was not practical in location description because the
coordinates in different passes were different. Instead, relative location information
185 was used in this study. That is, the o'clock and distance of a region relative to nipple
were used to describe the region location as a vector shown in Fig. 3. The derived
location criteria were clock, relative distance, and distance to nipple as the
descriptions in the following.



190 Fig. 3. The blue arrow indicates a vector expressing the location of a region bounded
by a red circle relative to the nipple (yellow point).

Clock information of a region can be obtained by calculating the relative position to nipple in coronal view. Taking the nipple as the origin point, the angle between the vector of a region A and the horizon was calculated to obtain the region's clock (Fig. 4). The clock difference of two regions was then calculated to be $Clock_{diff}$.

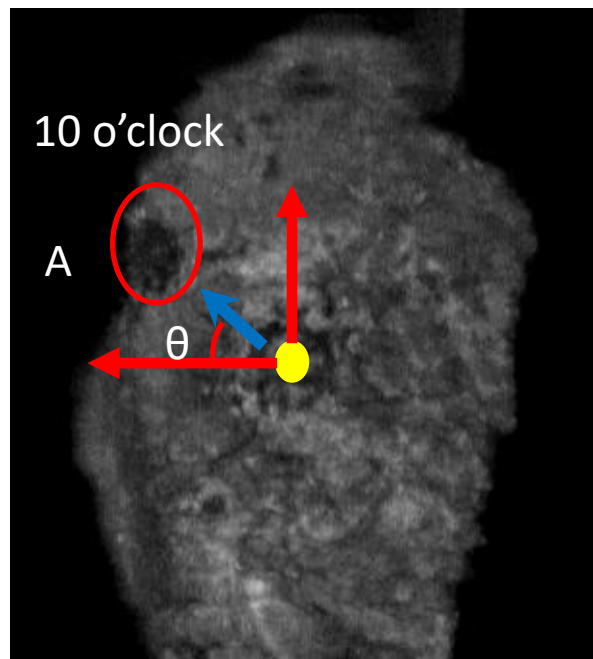
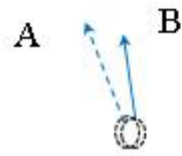
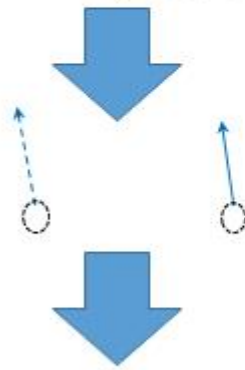
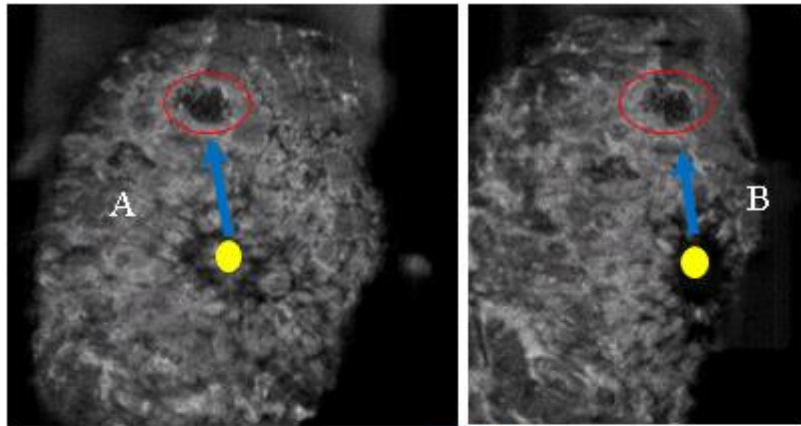


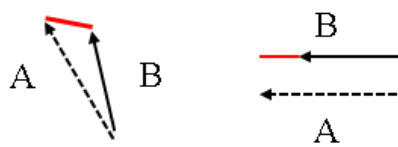
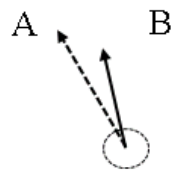
Fig. 4. The coordination on row and slice plane (C view). The blue arrow indicates a vector from the nipple (yellow point) to the region (red circle). The origin point is nipple. The tumor region in the figure is on 10 o'clock.

The other two location criteria of two regions in a mapping pair were relative distance ($RDistance_{diff}$) and distance to nipple ($Distance_{diff}$). As shown in Fig. 5(a), the correlation between the vectors of two regions, A and B, can be simulated by taking the nipple as the reference point. Relative distance (Fig. 5(b) left) of A and B is the Euclidean distance of their vectors. Distance to nipple (Fig. 5(b) right) is the length

difference of the two vectors relative to nipple.



(a)



(b)

210

215 Fig. 5. The location criteria are the correlations between the vectors of two regions, A and B. (a) The simulation of vector locations by using the nipple as the reference point. (b) Relative distance of A and B is the Euclidean distance of their vectors (left) and Distance to nipple is the length difference of the two vectors relative to nipple (right).

The threshold values of the location criteria including $Clock_{diff}$, $RDistance_{diff}$, and
220 $Distance_{diff}$ were determined according to the observation of the mapping pairs with the same regions assessed by the radiologist. Note that the transformation and displacement of breast tissues were unavioded during the scanning. The threshold values of the location criteria couldn't be zero. In the experiment, $Clock_{diff}=2$, $RDistance_{diff}=3$ cm, and $Distance_{diff}=2$ cm were used.

225

Quantitative Features

After location criteria, quantitative features including intensity, morphology, texture and location features were extracted from the remaining mapping pairs and combined in a classifier to distinguish between the same and different regions in each
230 pair. Table 1 lists a total of 20 quantitative features according to different categories. Detailed descriptions were stated in the following paragraphs.

Intensity features were I_STD_{diff} , I_Rank_{diff} , and I_NR_{diff} used to express the difference of tissue echogenicities in a mapping pair by gray-scale intensities. I_STD_{diff} was the difference of intensity standard deviation (SD). I_Rank_{diff} was the

235 difference of intensity rank¹⁰, the intensity magnitude of a region relative to other regions in an image. I_NR_{diff} is the other feature to calculate the difference of correlation which is the gradient between a region and its neighbor regions.

Morphology features were widely used in describing region shape in ABUS images¹¹. Vol_{diff} was the difference of the region volumes which were the essential properties of segmented regions. Cube level, $CubeL$, was the level of a region being cube calculated by dividing the maximum value between height and width with the slice number:

$$CubeL = \frac{MAX(R_H, R_W)}{R_S} \quad (3)$$

where R_H, R_W and R_S is the height, width and slice number of a region, respectively. In the comparison of regions, dividing the $CubeL$ difference by the $CubeL$ of AP region to obtain $CubeL_{diff_ratio}$ was a more useful feature to highlight the difference.

245 Image moments such as eigenvalue, major axis length, and minor axis length were also calculated to be the morphology features¹². Three measurements including raw moment, central moment and covariance matrix were defined first. For a 3-D image $I(x, y, z)$, the raw moment of order p, q, r is defined as:

$$M_{p,q,r} = \sum_{z=0}^{Z-1} \sum_{y=0}^{Y-1} \sum_{x=0}^{X-1} x^p y^q z^r I(x, y, z) \quad (4)$$

250 where X, Y, Z are the height, width, and depth. Pixels inside the region of $I(x, y, z)$ is

set to 1 and 0 for others. The central moment of order p, q, r is defined as:

$$\mu_{p,q,r} = \sum_{z=0}^{Z-1} \sum_{y=0}^{Y-1} \sum_{x=0}^{X-1} (x - \bar{x})^p (y - \bar{y})^q (z - \bar{z})^r I(x, y, z) \quad (5)$$

$$\bar{x} = M_{100}/M_{000} \quad (6)$$

$$\bar{y} = M_{010}/M_{000} \quad (7)$$

$$\bar{z} = M_{001}/M_{000} \quad (8)$$

where \bar{x} , \bar{y} , and \bar{z} are the centroid coordinates of a region. The covariance matrix is

defined as:

$$\begin{bmatrix} \mu'_{200} & \mu'_{110} & \mu'_{101} \\ \mu'_{110} & \mu'_{020} & \mu'_{011} \\ \mu'_{101} & \mu'_{011} & \mu'_{002} \end{bmatrix} \quad (9)$$

where the matrix elements are normalized second order central moments¹³. From the

255 matrix, three eigenvalues: λ_0 , λ_1 , and λ_2 were extracted to approximate the best-fit

ellipse. The major axis length, AL_{major} , and minor axis length, AL_{minor} , were formulated

by eigenvalues:

$$AL_{major} = 4\sqrt{\lambda_2} \quad (10)$$

$$AL_{minor} = 4\sqrt{\lambda_0} \quad (11)$$

The corresponding difference features were AL_{major_diff} and AL_{minor_diff} . Eccentricity is

the ratio of the lengths between two focal and the major axis of the ellipse:

$$Ecc = \sqrt{\frac{\lambda_1 - \lambda_0}{\lambda_1}} \quad (12)$$

260 The corresponding difference features was Ecc_{diff} .

Texture features are the spatial correlations between pixels in a region used to describe a specified pattern. The echogenic patterns in the ABUS images were quantified using the gray-scale co-occurrence matrix (GLCM)^{14, 15} in the experiment.

For an image I , a co-occurrence $N \times N \times N$ matrix M is constructed with the element defined as $P = [p(i, j, k | d, \theta)]$. Each element is the frequencies of three adjacent pixels with the intensity value i, j , and k in a distance d and angle θ . In the experiment, $N=64$, $d=1$, and $\theta=0^\circ, 45^\circ, 90^\circ, 135^\circ$. Six GLCM texture features are defined as follows:

$$\text{Entropy:} \quad f_1 = -\sum_k \sum_j \sum_i p(i, j, k | d, \theta) \log(p(i, j, k | d, \theta)) \quad (13)$$

$$\text{Correlation:} \quad f_2 = \frac{\sum_k \sum_j \sum_i (i - \mu_x)(j - \mu_y)(k - \mu_z) p(i, j, k | d, \theta)}{\sigma_x \sigma_y \sigma_z} \quad (14)$$

$$\text{Inverse Difference Moment:} \quad f_3 = \sum_i \sum_j \sum_k \frac{1}{1 + (i - j)^2 + (i - k)^2 + (j - k)^2} p(i, j, k | d, \theta) \quad (15)$$

$$\text{Inertia:} \quad f_4 = \sum_i \sum_j ((i - j)^2 + (i - k)^2 + (j - k)^2) p(i, j, k | d, \theta) \quad (16)$$

$$\text{Cluster Prominence:} \quad f_5 = \sum_i \sum_j (i + j + k - \mu_x - \mu_y - \mu_z)^4 p(i, j, k | d, \theta) \quad (17)$$

$$\text{Haralick's Correlation:} \quad f_6 = \frac{\sum_k \sum_i \sum_j (i \cdot j \cdot k) p(i, j, k | d, \theta) - \mu_x \mu_y \mu_z}{\sigma_x \sigma_y \sigma_z} \quad (18)$$

where $\mu_x, \mu_y, \mu_z, \sigma_x, \sigma_y$, and σ_z are mean and SD of the marginal distributions of $p(i, j, k | d, \theta)$. The statistical mean and SD of the six GLCM features were calculated to

be the texture features in this study.

Location features were the three location criteria mentioned above including

clock difference ($Clock_{diff}$), relative distance ($RDistance_{diff}$) and distance to nipple ($Distance_{diff}$). They were also used in the classifier for further discrimination.

275 **Statistical analysis**

The quantitative intensity, morphology, texture and location features mentioned above were combined in the binary logistic regression classifier¹⁶ to distinguish between the same and different regions in each pair. In feature selection, the lowest error rate of backward elimination in the trained classifier was the criterion to extract the most relevant subset of features. Leave-one-out cross-validation was used to validate the performance of the selected features. A case picked from the total K cases was used to test the model trained by the remaining $K-1$ cases. Each case was picked only once. After K times, the tested performances were averaged for a more generalized evaluation.

285 According to the ground truth assessed by the radiologist, each mapping pair was given a probability indicating its likelihood being the same regions after classification. Mapping pairs with higher probability than a threshold was the predicted positive mappings. Otherwise, they were regarded as predicted negative mapping pairs which were not determined to have the same regions by the classification model. In each mapping pair, the regions in AP were mapped by regions from MED or LAT because

the AP regions provided the least distortion and displacement of tumor location and characteristics. Therefore, if a region on MED or LAT is mapping to two or more AP regions with higher predicted probabilities than the defined threshold, only the highest mapping pair is chosen. On the other hand, the regions on AP can be mapped by more than one region on MED or LAT.

The performance of tumor mapping was evaluated by the mapping rate and error rate as defined below:

$$\text{Mapping Rate: } \frac{\text{number of correctly predicted positive mapping pairs}}{\text{number of positive mapping pairs}} \quad (19)$$

$$\text{Error Rate: } \frac{\text{number of incorrectly predicted negative mapping pairs}}{\text{number of negative mapping pairs}} \quad (20)$$

where positive and negative mapping pairs were the same regions and different regions recognized by the radiologist in the ground truth, respectively. The trade-offs between mapping rate and error rate were illustrated using the receiver operating characteristic (ROC) curve. The normalized area under the curve, Az, was used in ROC evaluation. Az was obtained using ROCKIT software (C. Metz, University of Chicago, Chicago, IL, USA).

305 **Results**

For the 511 detected regions in the CADe system, the original number of mapping pairs was 1506. After the location criteria, the number of mapping pairs was

reduced to 118 as shown in Table 1. According to the ground truth, they were 51 positive mapping pairs including 25 tumor and 26 non-tumor pairs and 67 negative mapping pairs. All mapping pairs with the same tumor regions were kept after location criteria.

Table 1 The number of mapping pairs after different location criteria

Location criteria	Number of mapping pairs
N/A	1506
Clock	439
Clock + Relative Distance	348
Clock + Relative Distance + Distance to Nipple	118

A total of 20 quantitative features were selected after backward elimination as shown in Table 2. The performance achieved by the selected features is listed in Table 3. The trade-offs between mapping and error rate was evaluated using the receiver operating characteristic (ROC) curve as shown in Fig. 6. The area under the ROC curve (A_z) is 0.9094.

Table 2 The selected features for tumor mapping

Category	Feature	Description
Intensity	I_STD_{diff}	Difference of intensity SD
	I_Rank_{diff}	Difference of intensity rank
	I_NR_{diff}	Difference of neighbor intensity
Morphology	Vol_{diff}	Difference of volume
	$CubeL_{diff_ratio}$	Difference of Cube level
	λ_{0_diff} , λ_{1_diff} , and λ_{2_diff}	Three eigenvalue differences
	AL_{major_diff}	Difference of major axis length
	AL_{minor_diff}	Difference of minor axis length

	<i>Ecc_{diff}</i>	Difference of ellipse eccentricity
Texture	<i>Entropy_{mean_diff}</i>	Difference of entropy mean
	<i>Correlation_{mean_diff}</i>	Difference of correlation mean
	<i>IDM_{mean_diff}</i>	Difference of inverse difference moment mean
	<i>IDM_{SD_diff}</i>	Difference of inverse difference moment SD
	<i>Inertia_{SD_diff}</i>	Difference of inertia SD
	<i>CP_{SD_diff}</i>	Difference of cluster prominence SD
	<i>HC_{mean_diff}</i>	Difference of Haralick correlation mean
Location	<i>RDistance_{diff}</i>	Difference of relative distance
	<i>Distance_{diff}</i>	Difference of distance to nipple

*SD= standard deviation

320

Table 3 The mapping rate and error rate for different region types in a mapping pair.

Region Type	Tumor Region (Mapping Rate/Error Rate)	Non-tumor Region (Mapping Rate/Error Rate)
Overall Mapping Rate/ Error Rate		
80.39% (41/51)/ 5.97%(4/67)	80.00% (20/25)/ 0.00% (0/25)	80.76% (21/26)/ 9.52% (4/42)
90.19% (46/51)/ 19.40%(13/67)	92.00% (23/25)/ 24.00% (6/25)	88.46% (23/26)/ 16.67% (7/42)
100.00% (51/51)/ 47.76%(32/67)	100.00% (25/25)/ 60.00% (15/25)	100.00% (26/26)/ 40.47% (17/42)

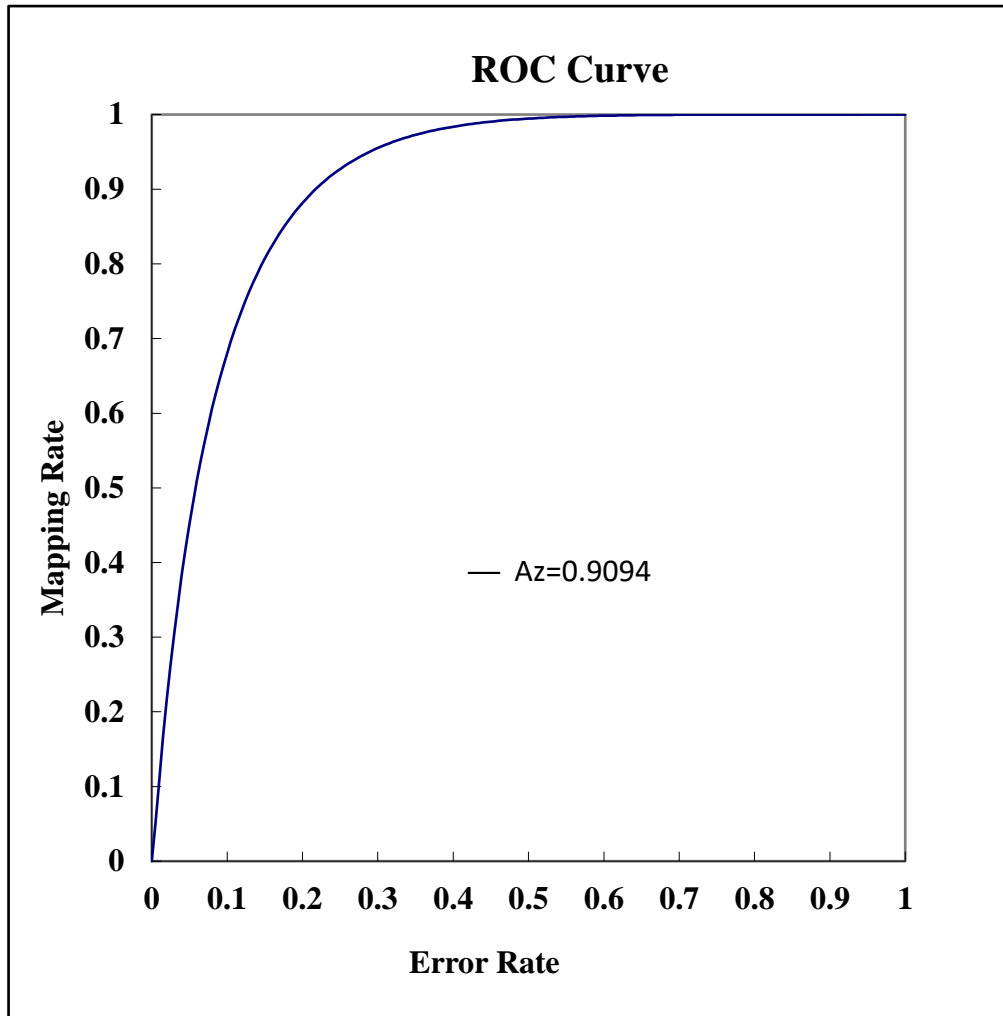


Fig. 6. The ROC curve of the mapping result

325 The distribution of correctly predicted positive mapping pairs with the same tumor regions is shown in Table 4. Under the mapping rate of 80%, the error rates are 0% which means no mapping pairs with different regions are misclassified. Simultaneously, 88% (15/17) benign tumors and 62.5% (5/8) malignant tumors in the positive mapping pairs were successfully predicted. Fig. 7 shows a correctly classified

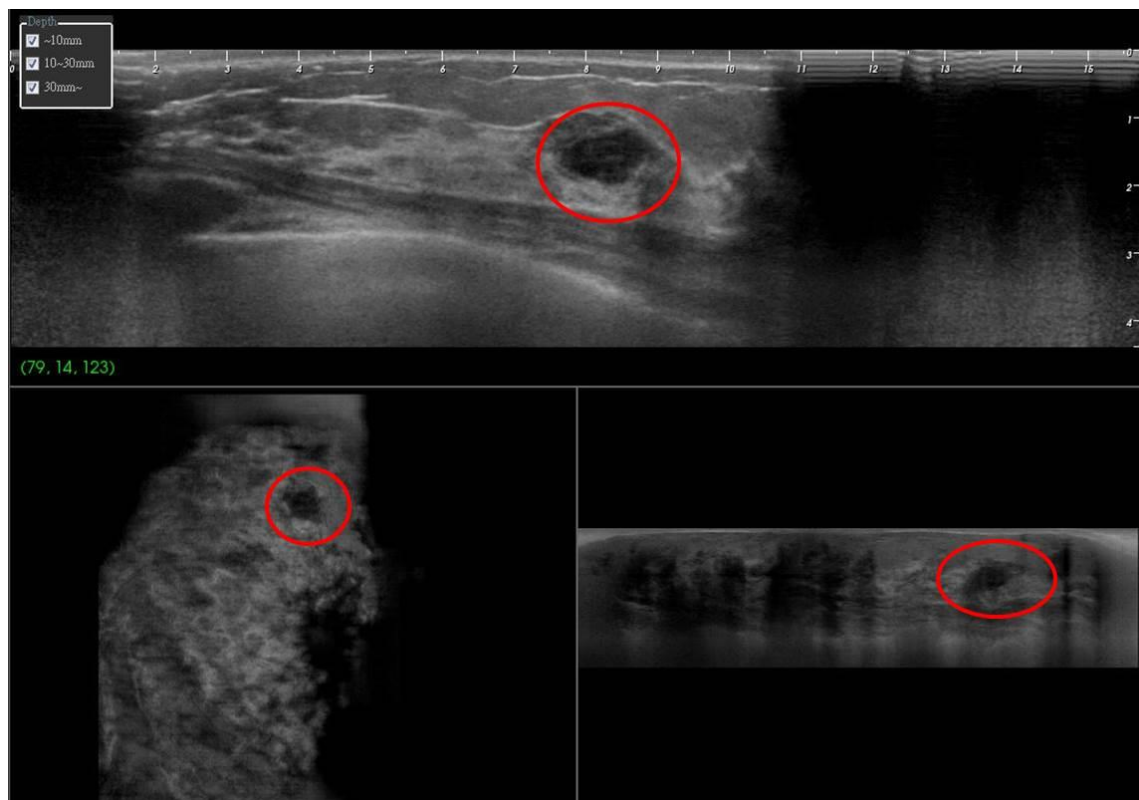
330 fibroadenoma case. The mapping pair of the true fibroadenoma in MED (Fig. 7 (a)) mapped to the same region in AP (Fig. 7 (b)) is correctly classified as a positive

mapping pair with the probability of 0.861 while the mapping pair to a shadow in AP (Fig. 7 (c)) is also correctly classified as a negative mapping pair with the probability of 0.001.

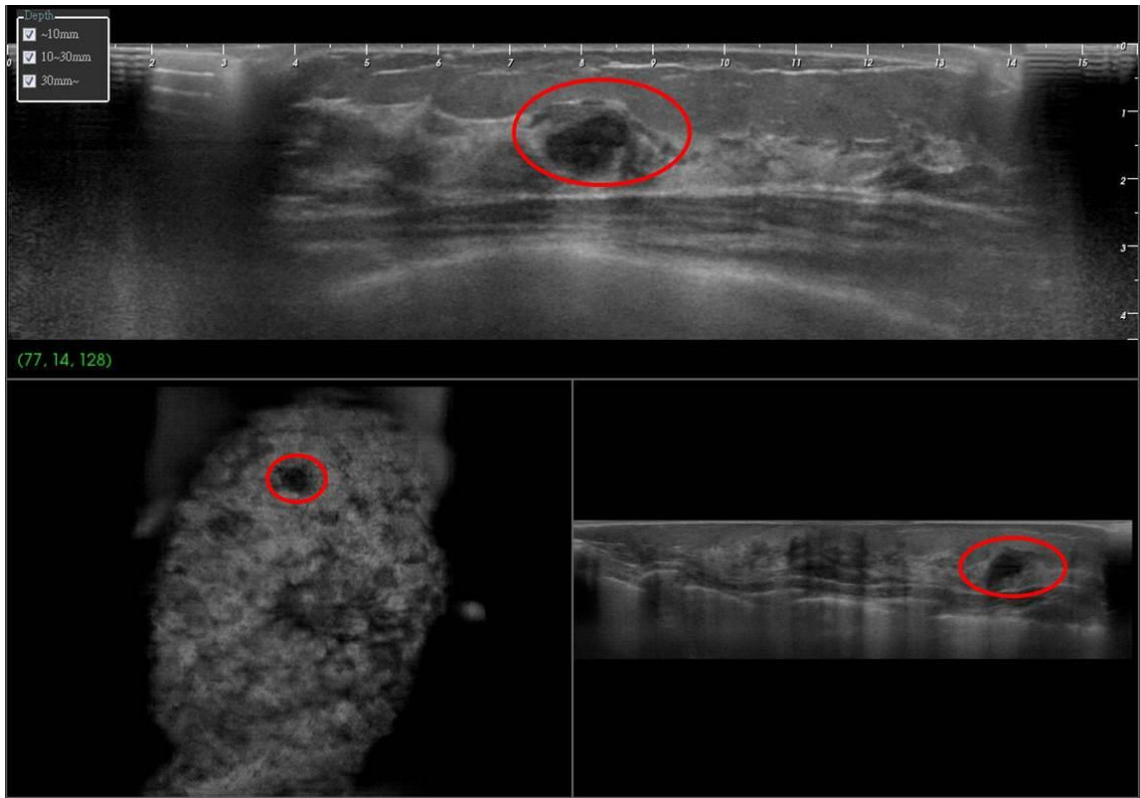
335

Table 4 The distribution of tumor sizes and pathologies at different mapping rates

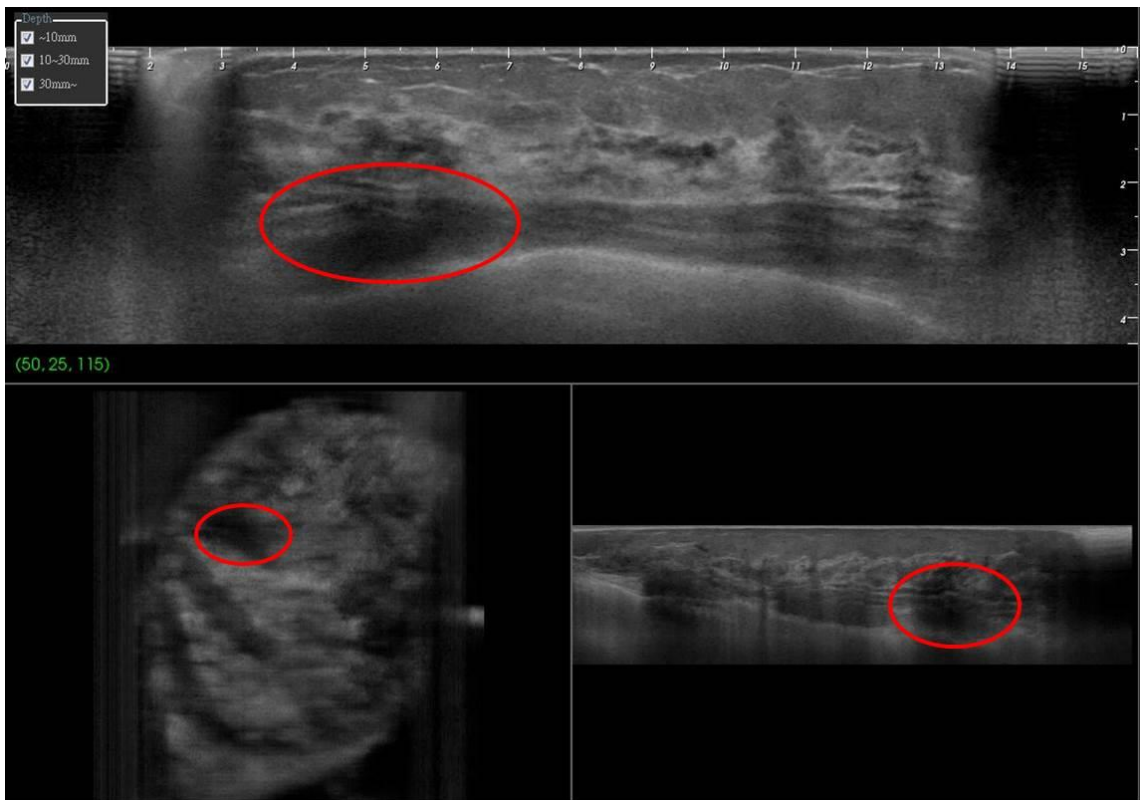
Mapping Rate (%)	Malignant (cm)				Benign (cm)			
	<1.0	1.0 – 2.0	2.0 – 3.0	>3.0	<1.0	1.0 – 2.0	2.0 – 3.0	>3.0
60	0	0	2	1	2	5	3	2
70	1	0	2	1	3	6	3	2
80	1	0	2	2	3	7	3	2



(a)



(b)



(c)

Fig. 7. Mapping pairs of a fibroadenoma case with red circles indicating the detected regions in axial, sagittal, and coronal view of the CADe system includes (a) A

340

345

350 true fibroadenoma in MED pass (b) The true fibroadenoma in AP pass (c) A shadow in AP pass. As a mapping result, the mapping pair of (a) and (b) is correctly classified as a positive mapping pair with the probability of 0.861 and the mapping pair of (a) and (c) is correctly classified as a negative mapping pair with the probability of 0.001.

Discussion

US is a useful modality to detect breast cancer in dense breasts^{6, 17, 18}. For the reproducibility and efficiency, ABUS is developed to automatically scan the whole breast without operator dependence. In the ABUS scanning, three passes including AP, MED, and LAT are performed to completely cover the breast tissues. Reviewing the thousands of 2D slices for a patient with two breasts is a time-consuming task to radiologists. Based on the detected result of a CADe system¹⁰, this study further took the overlappings between passes into consideration and proposed a tumor mapping algorithm to find the same regions in different passes. The use of location criteria reduced about 92% mapping pairs with different regions. In the further classification, 20 quantitative intensity, morphology, texture and location features were combined in the logistic regression model to achieve the mapping rate of 80.39% (41/51) with error rate of 5.97% (4/67) as shown in Table 3. For tumor regions, the mapping rate was 80.00% (20/25) with the error rate of 0.00% (0/25). For non-tumor regions, the mapping rate was 80.76% (21/26) and the error rate was 9.52% (4/42). In clinical use,

the tumor mapping rate of 80.00% means that radiologists don't need to manually find all the correspondences between tumors in different passes. The mapping algorithm can automatically provide the corresponding location information for 80% tumors
370 with error rate of 0%. Radiologists would save more time in finding the same tumors and take more time in interpreting the tumor characteristics for diagnosis.

Tan et al.¹⁹ proposed a method based on intensity, speculation, boldness, and contrast features to predict tumor locations from one pass to another pass. The ABUS images were obtained from the Siemens ACUSON S2000 ABVS in the Radboud
375 University Nijmegen Medical Center (Nijmegen, The Netherlands) and the Jules Bordet Institute (Brussels, Belgium). They achieved an average error= 15.64 ± 16.13 mm for location measurement. Rather than calculating the displacement only, this study extended the CADe system¹⁰ to the following tumor mapping in different passes. Combining the proposed mapping algorithm with an existed CADe system would
380 provide a more efficient and reliable procedure for ABUS examinations.

A limitation of the mapping algorithm is that if two regions are very close to the nipple, their clock difference must be very small. At this time, this mapping pair would not be filtered out by the other two criteria: relative distance and distance to nipple because the two criteria are also small. A possible solution is using adaptive
385 thresholds for different distances between mapping pairs and the corresponding nipple.

More observation and experiments in the future study will be useful to explore more reliable location criteria and quantitative features in improving the mapping rate of the tumor mapping algorithm.

390 **Acknowledgments**

The authors thank the Ministry of Science and Technology (MOST 103-2221-E-002-170-MY3), Ministry of Economic Affairs (100-EC-17-A-19-S1-164), Department of Health (DOH102-TD-C-111-001), and Ministry of Education (AE-00-00-06) of the Republic of China for the financial support.

395

References

- ¹ R. Siegel, D. Naishadham, A. Jemal, "Cancer statistics, 2013," *CA: a cancer journal for clinicians* **63**, 11-30 (2013).
- ² E.A. Sickles, R. Filly, P. Callen, "Benign breast lesions: ultrasound detection
400 and diagnosis," *Radiology* **151**, 467-470 (1984).
- ³ T.M. Kolb, J. Lichy, J.H. Newhouse, "Comparison of the performance of
screening mammography, physical examination, and breast us and evaluation of
factors that influence them: an analysis of 27,825 patient evaluations1,"
Radiology **225**, 165-175 (2002).
- ⁴ K.M. Kelly, J. Dean, W.S. Comulada, S.-J. Lee, "Breast cancer detection using
405 automated whole breast ultrasound and mammography in radiographically
dense breasts," *European radiology* **20**, 734-742 (2010).
- ⁵ K. Flobbe, P. Nelemans, A. Kessels, G. Beets, M. Von Meyenfeldt, J. Van
Engelshoven, "The role of ultrasonography as an adjunct to mammography in
410 the detection of breast cancer: a systematic review," *European Journal of Cancer*
38, 1044-1050 (2002).
- ⁶ V. Corsetti, A. Ferrari, M. Ghirardi, R. Bergonzini, S. Bellarosa, O. Angelini, C.
Bani, S. Ciatto, "Role of ultrasonography in detecting mammographically occult
breast carcinoma in women with dense breasts," *La radiologia medica* **111**,

- 415 440-448 (2006).
- ⁷ K.J. Taylor, C. Merritt, C. Piccoli, R. Schmidt, G. Rouse, B. Fornage, E. Rubin, D. Georgian-Smith, F. Winsberg, B. Goldberg, "Ultrasound as a complement to mammography and breast examination to characterize breast masses," *Ultrasound in medicine & biology* **28**, 19-26 (2002).
- 420 ⁸ P. Crystal, S.D. Strano, S. Shcharynski, M.J. Koretz, "Using sonography to screen women with mammographically dense breasts," *American Journal of Roentgenology* **181**, 177-182 (2003).
- ⁹ T. Tan, B. Platel, R. Mus, L. Tabar, R.M. Mann, N. Karssemeijer, "Computer-aided detection of cancer in automated 3d breast ultrasound," *Medical Imaging, IEEE Transactions on* **32**, 1698-1706 (2013).
- 425 ¹⁰ C.-M. Lo, R.-T. Chen, Y.-C. Chang, Y.-W. Yang, M.-J. Hung, C.-S. Huang, R.-F. Chang, "Multi-dimensional Tumor Detection in Automated Whole Breast Ultrasound using Topographic Watershed," *Medical Imaging, IEEE Transactions on* **33**, 1503-1511 (2014).
- 430 ¹¹ W.K. Moon, C.-M. Lo, J.M. Chang, C.-S. Huang, J.-H. Chen, R.-F. Chang, "Computer-aided classification of breast masses using speckle features of automated breast ultrasound images," *Medical physics* **39**, 6465 (2012).
- ¹² M.-K. Hu, "Visual pattern recognition by moment invariants," *Information*

Theory, IRE Transactions on **8**, 179-187 (1962).

435 ¹³ F.A. Sadjadi, E.L. Hall, "Three-dimensional moment invariants," Pattern Analysis and Machine Intelligence, IEEE Transactions on, 127-136 (1980).

¹⁴ W.K. Moon, C.-M. Lo, C.-S. Huang, J.-H. Chen, R.-F. Chang, "Computer-aided diagnosis based on speckle patterns in ultrasound images," Ultrasound in medicine & biology **38**, 1251-1261 (2012).

440 ¹⁵ R.M. Haralick, K. Shanmugam, I.H. Dinstein, "Textural features for image classification," Systems, Man and Cybernetics, IEEE Transactions on, 610-621 (1973).

¹⁶ D.W. Hosmer, S. Lemeshow, *Applied logistic regression. 2nd edition.* (Wiley, New York, 2000).

445 ¹⁷ S.S. Kaplan, "Clinical Utility of Bilateral Whole-Breast US in the Evaluation of Women with Dense Breast Tissue¹," Radiology **221**, 641-649 (2001).

¹⁸ K. Uchida, A. Yamashita, K. Kawase, K. Kamiya, "Screening ultrasonography revealed 15% of mammographically occult breast cancers," Breast Cancer **15**, 165-168 (2008).

450 ¹⁹ T. Tan, B. Platel, M. Hicks, R.M. Mann, N. Karssemeijer, "Finding lesion correspondences in different views of automated 3D breast ultrasound," in SPIE Medical Imaging, pp. 86701N-86701N-6 (2013).

